# Direct visualization of dark exciton condensates in moiré superlattices

**Huan Liu**
Tsinghua University
**Jiangcai Wang**
Tshinghua University
**Shihong Chen**
Guangxi University
**Zejun Sun**
Tshinghua University
**Haowen Xu**
University of Science and Technology Beijing
**Yishu Han**
Tshinghua University
**Chong Wang**
Tshinghua University
**Huixian Liu**
Tshinghua University
**Li Huang**
Tsinghua University
**Dameng Liu** ( ldm@tsinghua.edu.cn )
Tshinghua University
**Jianbin Luo**
Tsinghua University

**Article**

**Keywords:**

**Posted Date:** October 7th, 2022

**DOI:** https://doi.org/10.21203/rs.3.rs-2104824/v1

# Direct visualization of dark exciton condensates in moiré superlattices

Huan Liu[1], Jiangcai Wang[1], Shihong Chen[2], Zejun Sun[1], Haowen Xu[3], Yishu Han[1], Chong Wang[1], Huixian Liu[1], Li Huang[1], Dameng Liu[1,*] & Jianbin Luo[1,*]

[1] State Key Laboratory of Tribology, Tsinghua University, Beijing, China
[2] School of Resources, Environment and Materials, Guangxi University, Nanning 530004, China
[3] Institue for Advanced Materials and Technology, University of Science and Technology Beijing, Beijing, China

*E-mail: ldm@tsinghua.edu.cn; luojb@mail.tsinghua.edu.cn

**Moiré superlattices have emerged as an unprecedented manipulation tool for engineering correlated quantum phenomena in van der Waals heterostructures[1-4]. With moiré potentials as a naturally configurable solid-state that sustains high exciton density, interlayer excitons in transition metal dichalcogenide (TMDC) heterostructures are expected to achieve high-temperature exciton condensation and related superfluidity[5]. However, the exciton condensation is usually optically inactive due to the finite momentum of interlayer excitons. The experimental observation of dark exciton condensation in moiré potentials remains challenging with traditional optical techniques. Here we directly visualize the dark-exciton condensation in twisted TMDC heterostructures using femtosecond transient absorption microscopy. We observe a quantum transition from classical exciton gas to exciton condensation by imaging temperature-dependent exciton transport. With decreasing temperature, exciton diffusion rates exhibit an accelerating downwards trend under a critical degeneracy temperature, indicative of exciton condensation. This result is attributed to moiré potentials drastically suppressing exciton transport to promote exciton condensation. The ability to image exciton condensates opens the door to quantum information processing[6] and high-precision metrology in moiré superlattices.**

As bosons, excitons can collapse at sufficiently low temperature into a Bose-Einstein condensate state. In this regime, excitons flow without energy dissipation and friction, which makes excitons an ideal platform for designing low-dissipation electronic devices and achieving quantum computers[6-8]. The boson degeneracy temperature $T_d$ is determined by their density $n$ and effective mass $m^*$: $T_d = \frac{2\pi\hbar^2}{k_B g}\frac{n}{m^*}$. A Bose-Einstein condensate was first achieved with ultracold alkali atoms at ~100 nK (ref 9). With a much smaller mass, indirect excitons in bilayer GaAs have a degeneracy temperature below a few Kelvin[10-13]. However, the corresponding higher temperature is limited by their small exciton binding energy (4-10 meV)[14, 15], which leads to low exciton densities. Alternatively, interlayer excitons in transition metal dichalcogenide heterostructures have a large exciton binding energy (~100 meV)[16-19], in which excitons condense at a high temperature (>100 K) and form into a superfluid[20-24].

An obstacle to achieving a high degeneracy temperature in TMDC heterostructures is sustaining a high exciton density. However, the interlayer excitons carry a permanent dipole moment because the electron and hole reside in different TMDC layers, leading to a strong repulsive dipole-dipole interaction. The strong dipolar repulsion always results in a fast-spatial free expansion of excitons, quickly reducing the exciton density below the critical value for exciton quantum degeneracy. To solve this issue, the periodic moiré superlattices inherent to TMDC heterostructures[3, 25] have been shown to efficiently trap interlayer excitons, preventing exciton expansion to sustain a high exciton density[17, 26-29]. This spatially confining potential provides a naturally configurable solid-state for increasing the exciton condensate critical temperature, analogous to ultracold atoms in optical lattices[30, 31] or GaAs bilayer excitons in artificial lattices[32, 33]. Therefore, the moiré potential is expected to be used for accurately manipulating exciton condensates and exploring quantum state transitions in TMDC heterostructures[24]. However, obtaining experimental evidence of moiré-potential modulated exciton condensates remains challenging, limited by the direct optical inactivity measurement of dark-state exciton condensates[5, 34] with common photoluminescence (PL) spectrum techniques[22, 35].

In this study, we experimentally visualize the dark exciton condensate in twisted $WS_2$/h-BN/$WSe_2$ heterostructures using transient absorption microscopy (TAM), which can monitor the non-luminescence signal (Fig. 1a). We can directly image the ultrafast dynamics of exciton transport to reveal the phase transition from classic exciton gas to exciton condensation. Above the critical exciton degeneracy temperature (Fig. 1c), excitons are in the classic exciton gas regime with fast transport compared with the initial excitation spot (Fig. 1b). This process mainly depends on the thermal activation energy and exhibits a linear decreasing diffusion rate with decreasing temperature. In contrast, when excitons are in the condensate state, exciton diffusion is constrained due to moiré potentials (Fig. 1d), leading to an accelerating downwards trend with a quadratic function relationship. Importantly, we find that although moiré potentials can promote exciton degeneracy by sustaining a high exciton density, they limit the critical transition temperature by increasing the exciton effective mass. These results provide a crucial guideline for investigating excitonic condensation and superfluidity.

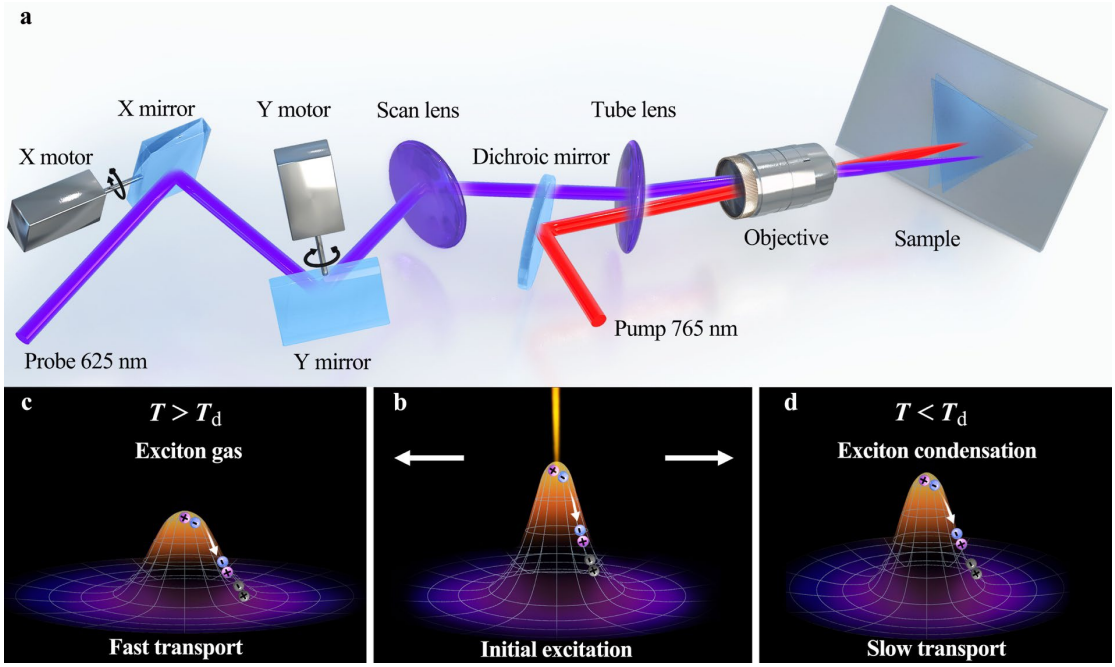


**Fig. 1 | Schematics of transient absorption microscopy and exciton quantum phase transition. a**, Femtosecond transient absorption microscopy is based on a pump-probe spectrum to detect exciton condensation by imaging temperature-dependent exciton transport. **b**, Exciton density distribution at an initial excitation state. **c**, Excitons are in a classical exciton gas regime when $T > T_d$, exhibiting a fast transport compared with

the initial excitation spot. **d**, Excitons enter into an exciton condensation regime when $T < T_d$, where a slow transport to sustain a high exciton density.

**Dark excitons in $WS_2$/h-BN/$WSe_2$ twisted heterostructures**

We fabricated $WS_2$/h-BN/$WSe_2$ twisted heterostructures (Fig. 2a) on a sapphire substrate by stacking two chemical-vapour-deposition grown monolayer TMDC samples and a monolayer h-BN film. The Raman spectrum is used to verify the heterostructure region (Supplementary Fig. 1). Their twist angle $\theta$ is obtained by measuring the angle between two sides of triangles. Owing to the type-II band alignment of $WSe_2$ and $WS_2$, electrons and holes generated in the heterostructure would accumulate in $WS_2$ and $WSe_2$, respectively, and form bosonic bound states. Furthermore, the interlayer twist and lattice-constant mismatch lead to moiré superlattices in the real-space arrangement (Fig. 2b), with a moiré period of $a_M$ (Supplementary Note 1). Their corresponding moiré potentials can cause a spatial modulation of the exciton energy[28, 36-40] (Supplementary Note 2), resulting in potential saddles and wells (Fig. 2c). The two-dimensional moiré potential distribution is shown in Supplementary Fig. 2. As a result, the lowest-energy excitons lie in their local minima of moiré potentials.

Another essential effect of the moiré superlattice is related to the optical activity of interlayer excitons. Namely, the interlayer twist makes excitons indirect in momentum space with a finite momentum $Q_m = K_c - K_v$ (Fig. 2d), resulting from the relative rotation of the Brillouin zones associated with each monolayer[26]. Therefore, the PL intensity of interlayer excitons sensitively depends on interlayer twists. For example, when the twist angle is ~0° or 60°, the location of exciton light cones exists at small kinematic momenta, in which interlayer excitons can directly interconvert with photons[19, 41]. In our study, to preserve an effective moiré potential, we focus on the small twist $\theta \sim 1°$ case that cannot radiatively recombine at low temperatures.

In addition to the interlayer twist, the possibility of optical activity also depends on the thermal distribution of excitons. Fig. 2e illustrates the momentum of the lowest-

energy interlayer excitons ($Q_m$) located away from the optically active region. The radiative possibility increases with increasing temperature, resulting from a broadened thermal distribution that increases the overlap with the light cone. Because the exciton condensate mainly occupies the lowest-energy state corresponding to the momentum-forbidden dark exciton[42], once the thermal fluctuation is ignored below the degeneracy temperature, the interlayer exciton cannot directly emit light. Thus, exciton condensation occurs in the moiré potential wells with dark states in our heterostructures.

Moreover, to allow for exciton condensates at sizable temperatures, the h-BN inserted between $WS_2$ and $WSe_2$ is necessary for suppressing the interlayer tunnelling [20]. Therefore, with the help of thermal activity at room temperature, the indirect excitons exhibit a long lifetime of radiative recombination in $WS_2$/h-BN/$WSe_2$ heterostructures (Fig. 2f). The long lifetime $\tau$ = 2.35 ns (extracted from PL decay profiles in Supplementary Fig. 3) enables the creation of high exciton density $n=P\tau$ with low laser power $P$, avoiding lattice or exciton overheating[21]. Meanwhile, the long exciton lifetime is evidence of the good contact quality in our heterostructures. Similar results are observed from the other sample (Supplementary Fig. 4).

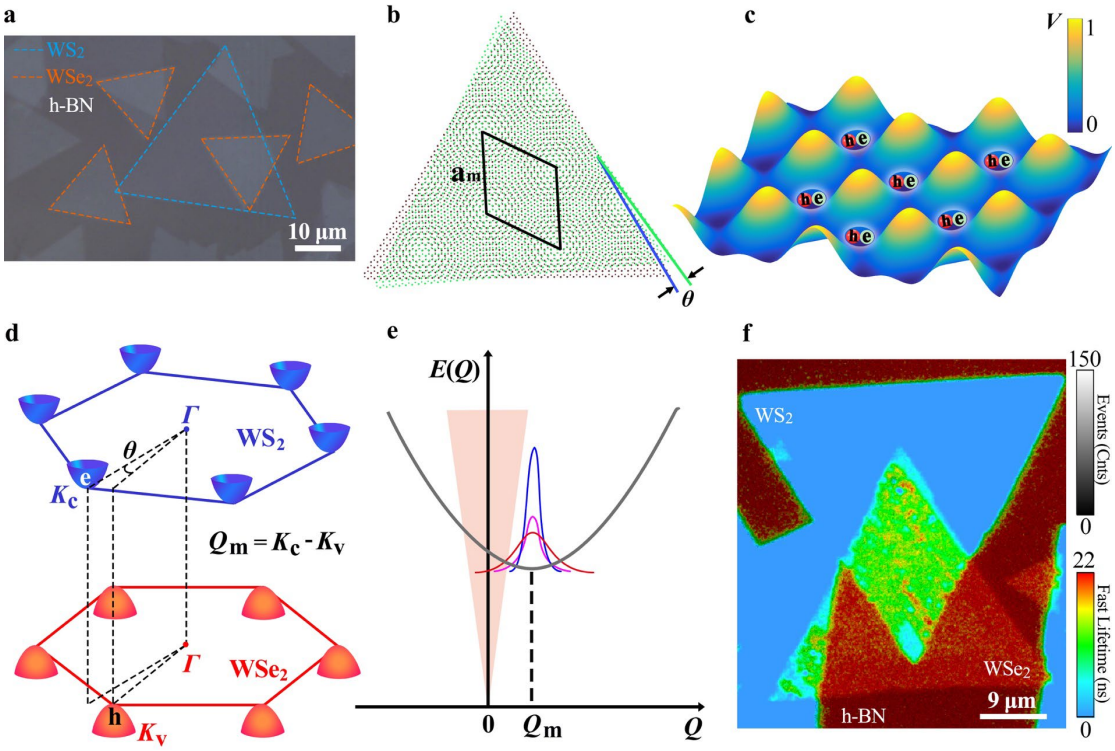


**Fig. 2 | Lowest-energy dark exciton state in moiré potentials. a**, Optical image of

CVD-grown $WS_2$/h-BN/$WSe_2$ twisted heterostructures on a sapphire substrate. **b**, Real space arrangement of the monolayer $WS_2$ and $WSe_2$ with a small twist angle $\theta$. The resulting moiré superlattice is marked in black. **c**, Moiré potentials trap interlayer excitons in the local minima. **d,** Brillouin zones of the monolayer $WSe_2$ (red) and $WS_2$ (blue). Their interlayer twist angle $\theta$ leads to a finite momentum mismatch $Q_m = K_c - K_v$. Interlayer exciton transition changes from direct to indirect. **e**, Dispersion of interlayer excitons with a small twist angle (grey line) and the photon dispersion (orange shaded region). Their intersection indicates the optically active exciton region. The other curves denote the thermal distribution of excitons with different temperatures. **f**, PL lifetime imaging pictures of interlayer excitons in the $WS_2$/h-BN/$WSe_2$ heterostructure at room temperature.

**Imaging exciton transport by ultrafast microscopy**

To visualize the spatial and temporal evolution of dark excitons, we employ femtosecond transient absorption microscopy to image exciton transport (methods and the schematic of TAM in Supplementary Fig. 5). The pump beam at 1.62 eV is used to purely excite electrons in $WSe_2$, because this energy lies below the lowest interband resonance of $WS_2$ (as shown in the energy band arrangement in Supplementary Fig. 6). Following electrons that are excited in $WSe_2$, electrons transfer to the conduction band of $WS_2$ in a few hundred femtoseconds[43] and subsequently form interlayer excitons. The pump power is 0.26 μJ/cm$^2$ to excite the interlayer excitons with an initial concentration $n_0 \sim 1 \times 10^{12}$ cm$^{-2}$ (Supplementary Note 3), which falls within the reasonable range for achieving exciton condensates and avoiding the complications arising from exciton-exciton annihilation[44]. Then, a probe beam at 1.98 eV is used to track the electron dynamics in the conduction band minimum of $WS_2$, namely, the interlayer exciton dynamics[45]. The probe reflection change $\triangle R$ (x, y, t) induced by the pump is proportional to the interlayer exciton density $n$ (x, y, t).

To acquire ultrafast exciton transport dynamics, the pump beam is fixed, and the probe beam scans the sample using a galvanometer at different pump-probe delay times. Fig. 3(a-f) present the representative time evolution images of two-dimensional exciton

transport in $WS_2$/h-BN/$WSe_2$ heterostructures at the temperature T=43 K. To quantitatively describe the exciton transport, we assume radial symmetry and a Gaussian distribution of the excited interlayer excitons. At the initial time, the interlayer excitons are created by a pump beam of ~1 μm comprising a Gaussian distribution of $n(x, 0)= n_0 \exp\left(-\frac{x^2}{\sigma_0^2}\right)$. With an increasing pump-probe delay time, excitons expand away from the initial volume. Fig. 3g shows the time-dependent exciton population profiles as a function of the pump-probe distance *x*, which are fitted by a Gaussian distribution of $n(x, t)= n_t \exp\left(-\frac{x^2}{\sigma_t^2}\right)$ (solid lines). Owing to the long radiative lifetime of interlayer excitons, we only monitor the exciton transport before 100 ps, avoiding the exciton transport length that exceeds the size of the samples. Moreover, the resolution of exciton transport beyond the diffraction limit can be observed by TAM with a ~60 nm spatial resolution (Supplementary Note 4). The high spatial resolution allows the visualization of exciton transport in an ultrafast time range.

To further explain the interlayer exciton transport dynamics, Fig. 3h shows the temporal dependence of $\sigma_t^2 - \sigma_0^2$, which exhibits a sublinear beheviour. This presents a striking contrast with intralayer exciton transport[46], in which only the population gradient drives the exciton transport, leading to a linear temporal dependence of $\sigma_t^2 - \sigma_0^2$. Here, we observe an initial fast-driven exciton expansion and a later slow exciton diffusion in this experiment. Similar sublinear behaviours have been observed when the exciton density is below the Mott transition density[45, 47], which are assigned to deep moiré potentials and strong repulsive exciton-exciton interactions, respectively. In our case, owing to the small twist, we cannot neglect the moiré potential effect and need to consider the effect both of them on interlayer exciton transport. The moiré effect can be verified by imaging the exciton transport dynamics under the low temperature T=30 K when the thermal fluctuations can be ignored (Supplementary Fig. 7), in which the exciton transport is significantly impeded by moiré potentials.

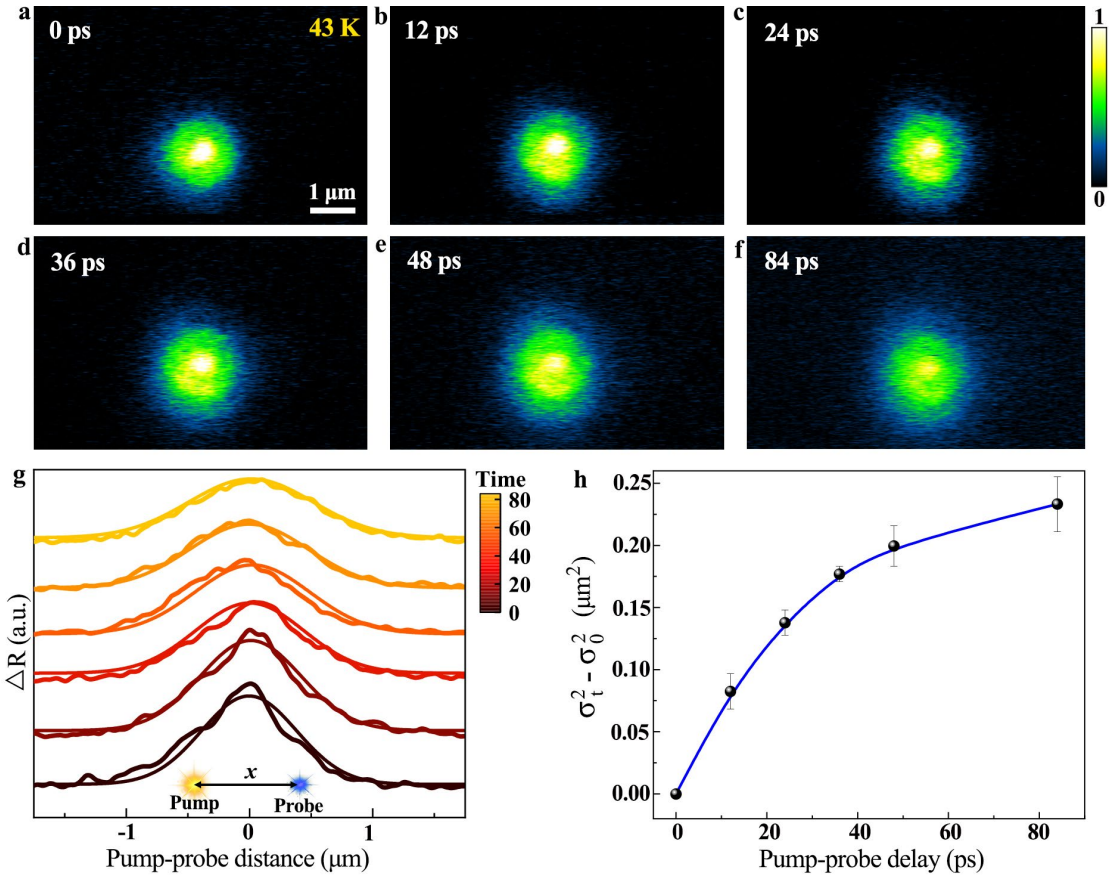


**Fig. 3 | Imaging exciton transport by ultrafast microscopy. a-f**, Two-dimensional transient absorption microscopy images of $WS_2$/h-BN/$WSe_2$ heterostructure at different pump-probe delay times at 43 K. The pump photon energy is 1.62 eV to excite electrons in $WSe_2$, and the probe photon energy is 1.98 eV to monitor electrons in $WS_2$. **g**, Exciton population profiles at different pump-probe delay times along the pump-probe distance $x$ through the TAM image center. Solid lines are fits by a Gaussian function to extract $\sigma_t^2$. **h**, A sublinear exciton transport behavior shown by the pump-probe delay dependence of $\sigma_t^2 - \sigma_0^2$. The solid line is the sublinear guideline. The error bars are the standard error of the fit of the exciton population profiles.

### Modelling of the degenerate exciton transport

To quantitatively identify the contributions of both the exciton-exciton interaction and moiré potential on exciton condensations, a nonlinear quantum diffusion model is used[48] (details in Supplementary Note 5):

$$\frac{\partial n(x,t)}{\partial t} = \nabla\left[D\nabla n(x,t) + D\left(\frac{m^*}{\pi\hbar^2}\right)\left(e^{\frac{T_d}{T}} - 1\right)\nabla[u_0 n(x,t) + V(x)]\right] - \frac{n(x,t)}{\tau}, \qquad (1)$$

where the first term $D\nabla n(x,t)$ describes the normal exciton diffusion due to the concentration gradient. The second term includes the drift flux $u_0 n(x,t)$ and moiré potential $V(x)$. And $u_0$ is the exciton-exciton interaction energy that includes dipolar repulsion and exchange interaction (Supplementary Note 6 and Note 7). In our case, since the h-BN spacer makes the separation *d* between two TMDC layers similar to the Bohr radius $a_B$ of indirect excitons, we neglect the exchange interaction[47]. The strong dipolar repulsion usually makes the exciton density drop below the critical degeneracy density much faster than the exciton recombination lifetime. Additionally, the repulsion energy becomes a heating source that slows the cooling process during the expansion via exciton-exciton scattering[49]. In contrast, the moiré potential $V(x)$ is expected to sustain a high exciton density and help excitons quickly cool down to the lattice temperature, raising the critical temperature of exciton condensations (Supplementary Note 8). This result occurs because that moiré potentials can effectively trap excitons at low temperatures (Supplementary Fig. 8), which significantly suppresses the fast exciton expansion and the density gradient. It is noted that $V(x)$ has a period of $a_{\mathrm{M}}$ that is much smaller than the pump beam size of ~1 μm, and $V(x)$ can be viewed as an averaged potential with 10 meV obtained from previous results[5].

Importantly, the temperature-dependent exciton coefficient $D$ can be used to identify the exciton condensation. Namely, for crossover from the classical exciton gas to quantum degeneracy, the relationship between exciton diffusion and temperature is given by

$$D = \begin{cases} \frac{k_0}{2}\frac{\hbar}{m^*}\frac{a_{\mathrm{B}}^2}{d^2}\left(\frac{\mu_x}{m^*}\right)^2\frac{T}{T_{\mathrm{d}}}, & T \gg T_{\mathrm{d}} \\ \frac{k_0\pi^2}{16}\frac{\hbar}{m^*}\frac{a_{\mathrm{B}}^2}{d^2}\left(\frac{\mu_x}{m^*}\right)^2\left(\frac{T}{T_{\mathrm{d}}}\right)^2, & T \ll T_{\mathrm{d}} \end{cases}, \tag{2}$$

where $\hbar$ is the reduced Planck's constant and $k_0$ is a numerical constant. In the classical limit, when $T \gg T_{\mathrm{d}}$, *D* is linearly correlated with temperature *T*. Alternatively, in the quantum degeneracy when $T \ll T_{\mathrm{d}}$, *D* exhibits a drastic reduction due to a nonclassical accumulation of low-energy excitons in moiré potentials, implying the exciton degeneracy state. Therefore, the appearance of the exciton condensate is supported by an anomalous temperature-dependent exciton diffusion.

**Quantum transition from exciton gas to exciton condensate**

To experimentally verify the exciton quantum phase transition, Fig. 4(a-c) shows the two-dimensional and three-dimensional TAM images under different temperatures at the same delay time t=24 ps. For the case T=43 K, in which the thermal activity cannot be neglected (Fig. 4a), the exciton density has a large expansion in real space. With decreasing temperatures, the thermal activity is suppressed. Moiré potentials greatly impede exciton transports and exciton densities are constrained in Fig. 4b and 4c, implying the quantum transition from exciton gas to exciton condensation. Notably, to avoid a complication in our experiment, we do not consider the effect of temperature on radiative lifetime $\tau$ because we only detect the ultrafast dynamics in 100 ps (much less than the exciton lifetime).

To determine the critical temperature of the quantum transition from classical exciton gas to exciton condensation, Fig. 4d presents $\sigma_t^2 - \sigma_0^2$ as a function of the pump-probe delay time at different temperatures. The exciton diffusion coefficient *D* is extracted by Equation (1). Furthermore, Fig. 4e shows the exciton diffusion coefficient as a function of temperature, where the solid line is the fit that uses Equation (2). The excitons experience two states with decreasing temperatures. First, the exciton diffusion coefficient shows a linear decrease with temperature, corresponding to a classic exciton gas state. In the gas regime, exciton diffusion can overcome moiré potentials through thermal activation and exciton-exciton repulsion[45, 48]. While the temperature is below a critical temperature of ~30 K, excitons are trapped in the moiré potential minima, leading to a sudden drop in the exciton diffusion coefficient and entering an exciton condensation state.

**Moiré potential-modulated exciton condensation**

We now turn to the limitation effect of moiré potentials on exciton condensations. Although the moiré potential can suppress exciton transport to obtain a high degeneracy temperature, the theoretical study has shown that large moiré potentials dramatically reduce the degeneracy temperature, mainly through the modulated exciton's effective mass[5, 33] (Supplementary Note 9). To evaluate the effective mass $m^*$ modulated by the

moiré potential, the Hamiltonian of the interlayer excitons in a moiré potential can be expressed as[5, 50]: $H = \frac{-\hbar^2}{2m}\frac{\partial^2}{\partial z^2} + V\sin^2(q_{\mathrm{M}}z)$, where the exciton motion is restricted to the direction $z$ of the moiré lattice, and its wave vector in the dimension is $q_M = \frac{\pi}{a_{\mathrm{M}}}$. Fig. 4f shows that the moiré potential exponentially increases the effective exciton mass. In a deep lattice potential[45], excitons are strongly localized in the moiré lattice sites, leading to an exponential increase in the exciton effective mass. In contrast, the excitons in shallow moiré potentials have a small effective mass.

The increasing exciton effective mass modulated by the moiré potential can substantially affect the exciton condensation critical temperature (Supplementary Fig. 9). In our heterostructure, because the moiré potential is highly screened by h-BN, the resulting moiré potential is ~10 meV (ref. 51), which leads to $m^*/m \sim 1.1$. Consequently, $T_{\mathrm{d}}$ reaches sizable temperatures, up to $T_{\mathrm{d}}$~30 K, which is consistent with our experimental observation. We emphasize that this result is in contrast with previous results[47] (which observe a large exciton transport area, > 5 um$^2$, at 4.6 K), since it is attributed to small moiré potentials with low exciton density and the inefficient PL-based optical probes for optically inactive excitons[5]. Therefore, when studying exciton condensation and its related superfluid in TMDC heterostructures, we need to weigh the effect of the moiré potential on exciton transport and effective mass.

In conclusion, we have directly visualized the dark exciton condensation in $WS_2$/h-BN/$WSe_2$ heterostructures using ultrafast transient absorption microscopy. By imaging temporal and spatial exciton transport, a quantum phase transition from classical exciton gas to degenerated exciton condensation is observed. Its critical transition temperature is around 30 K, at which moiré potentials suppress exciton expansion to sustain a high exciton density and raise the critical temperature. However, moiré potentials significantly limit the critical temperature by yielding an exponential increase in the exciton effective mass. Our results pave the way for future studies on high-temperature exciton superfluidity and quantum computers based on van der Waals moiré heterostructures.

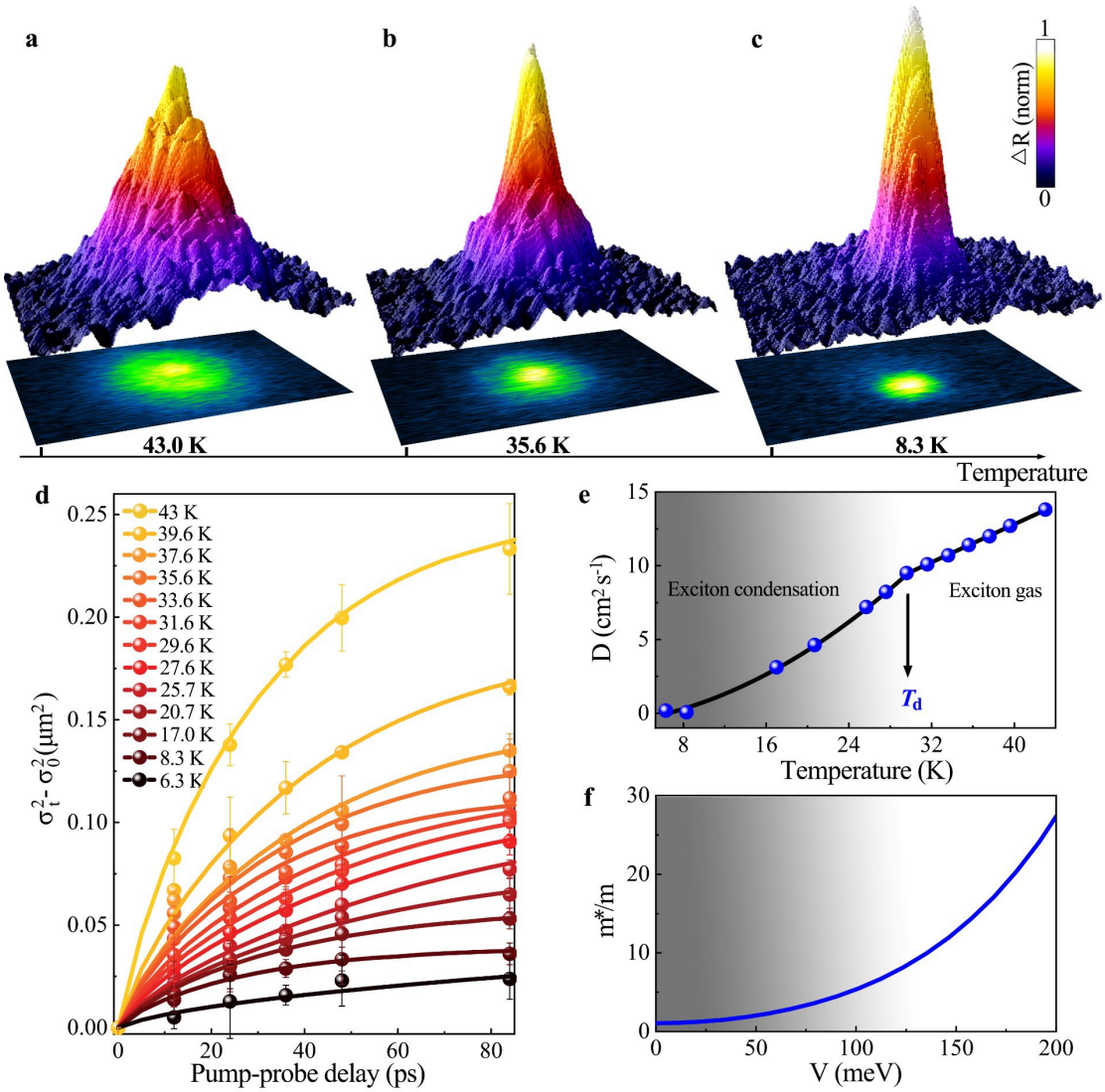


**Fig. 4 | Imaging exciton transport by ultrafast microscopy. a-c**, Two-dimensional and three-dimensional transient absorption microscopy images at different temperatures of 43.0 K, 35.6 K and 8.3 K, respectively. **d**, The pump-probe delay dependence of $\sigma_t^2 - \sigma_0^2$ with different temperatures. The solid lines are the fits using Equation (1) to extract diffusion coefficient *D*. The error bars are the standard error of the fit of the exciton population profiles. **e**, Temperature-dependent exciton coefficient *D*. The quantum degeneracy critical temperature $T_d$ is ~30 K. The solid lines are fits using Equation (2). **f**, Moiré potentials as a function of the ratio between exciton effective mass and exciton mass.

# Methods

## Sample preparation

Triangular monolayers of $WS_2$ and $WSe_2$ flake and monolayer h-BN film are produced by chemical vapor deposition growth. And $WS_2$/h-BN/$WSe_2$ heterostructures are prepared on sapphire substrates using PMMA-assisted transfer method. The interlayer twist angle is determined by comparing the orientation of two TDMC monolayers. This is because that the triangular TMDC flake has zigzag edges, which is sharp when the edges terminate with transition metal atoms[52].

## Optical measurements

Micro-Raman spectroscopy (Evolution, Horiba) is used to identify the region of $WS_2$/h-BN/$WSe_2$ heterostructures using a 532 nm wavelength laser (photon energy of 2.33 eV). Time-resolved PL measurements and fluorescence lifetime images are performed with an inverted fluorescence microscope (IX 83, Olympus) equipped with a time-correlated single-photon counting (PicoHarp 300, PicoQuant) at room temperature. The samples are excited by a picosecond pulsed diode laser at 485 nm using a 40×, 0.95 NA objective (UPLSAPO). The same objective collects PL signals, passes a 561 nm long-pass filter, and focuses on a photomultiplier. The data is analyzed by software (SymPhoTime 64), and every decay trace is extracted from more than 1000 photon counts.

## Femtosecond transient absorption microscopy

The schematic layout of the transient absorption microscopy step is shown in Supplementary Fig. 5. A Ti: Sapphire oscillator (Coherent) pumped by a Verdi diode laser is the light source (output at 765 nm, 25fs pulse-width, 80MHz repetition rate). Output from the oscillator is split into two beams. One is used as the pump pulse. The other output generates supercontinuum (SCKB-CARS, Thorlabs) and selects the wavelength 625 nm to serve as the probe beam. The polarization of pump and probe beams is made parallelly. The beams are focused on the sample with an objective (LMPLFLN 100 X, 0.8 NA, Olympus), and the pump and probe beams are spatially overlapped at the sample. The sample is mounted in a continuous-flow liquid helium cryostat (RC102-CFM, CIA). The reflectance signal is collected by the same objective,

and the probe is detected with an avalanche photodiode (APD, C12702-04, Hamamatsu). Pump-induced changes in the probe reflectance (ΔR) are measured by modulating the pump beam at 1 MHz with an acousto-optic modulator (AOM, 3080-125, Gooch Housego). The output of the APD is monitored with a lock-in amplifier (HF2LI, Zurich Instruments). The pump-probe delay time is controlled with a mechanical translation stage (DDS600-E/M, Thorlabs). For morphological TAM imaging, a 2D galvanometer (GVS012, Thorlabs) is used to scan the probe beam relative to the pump beam in space.

## Data availability

The data that support the findings of this study are available from the corresponding authors upon reasonable request.

## Acknowledgments

This work is supported by the National Natural Science Foundation of China (No. 52105195, 52075284, 11890672 and 52205209), the Defense Industrial Technology Development Program (JCKY2020110B007), and the Postdoctoral Research Foundation of China (No. 2020M680528 and BX2021151).

## Competing interests

The authors declare no competing financial interests.

# References

1. Li W, Qian X, Li J. Phase transitions in 2D materials. *Nature Reviews Materials*, (2021).
2. Zhu Q, Tu MW-Y, Tong Q, Yao W. Gate tuning from exciton superfluid to quantum anomalous Hall in van der Waals heterobilayer. *Science Advances* **5**, eaau6120 (2019).
3. Andrei EY*, et al.* The marvels of moiré materials. *Nature Reviews Materials* **6**, 201-206 (2021).
4. Andrei EY, MacDonald AH. Graphene bilayers with a twist. *Nature Materials* **19**, 1265-1275 (2020).
5. Lagoin C, Dubin F. Key role of the moiré potential for the quasicondensation of

interlayer excitons in van der Waals heterostructures. *Physical Review B* **103**, L041406 (2021).

6. Sager LM, Smart SE, Mazziotti DA. Preparation of an exciton condensate of photons on a 53-qubit quantum computer. *Physical Review Research* **2**, 043205 (2020).
7. Graham TM*, et al.* Multi-qubit entanglement and algorithms on a neutral-atom quantum computer. *Nature* **604**, 457-462 (2022).
8. Bluvstein D*, et al.* A quantum processor based on coherent transport of entangled atom arrays. *Nature* **604**, 451-456 (2022).
9. Anderson MH, Ensher JR, Matthews MR, Wieman CE, Cornell EA. Observation of Bose-Einstein condensation in a dilute atomic vapor. *Science* **269**, 198-201 (1995).
10. Dang S, Anankine R, Gomez C, Lemaître A, Holzmann M, Dubin F. Defect proliferation at the quasicondensate crossover of two-dimensional dipolar excitons trapped in coupled gaas quantum wells. *Physical Review Letters* **122**, 117402 (2019).
11. Anankine R*, et al.* Quantized vortices and four-component superfluidity of semiconductor excitons. *Physical Review Letters* **118**, 127402 (2017).
12. High AA*, et al.* Spontaneous coherence in a cold exciton gas. *Nature* **483**, 584-588 (2012).
13. High AA, Leonard JR, Remeika M, Butov LV, Hanson M, Gossard AC. Condensation of excitons in a trap. *Nano Letters* **12**, 2605-2609 (2012).
14. Grosso G*, et al.* Excitonic switches operating at around 100 K. *Nature Photonics* **3**, 577-580 (2009).
15. Szymanska MH, Littlewood PB. Excitonic binding in coupled quantum wells. *Physical Review B* **67**, 193305 (2003).
16. Mak KF, Shan J. Photonics and optoelectronics of 2D semiconductor transition metal dichalcogenides. *Nature Photonics* **10**, 216-226 (2016).
17. Rivera P, Yu H, Seyler KL, Wilson NP, Yao W, Xu X. Interlayer valley excitons in heterobilayers of transition metal dichalcogenides. *Nature Nanotechnology* **13**, 1004-1015 (2018).
18. Rivera P*, et al.* Observation of long-lived interlayer excitons in monolayer $MoSe_2$-$WSe_2$ heterostructures. *Nat Commun* **6**, 6242 (2015).
19. Rivera P*, et al.* Valley-polarized exciton dynamics in a 2D semiconductor heterostructure. *Science* **351**, 688-691 (2016).
20. Wang Z*, et al.* Evidence of high-temperature exciton condensation in two-dimensional atomic double layers. *Nature* **574**, 76-80 (2019).
21. Fogler MM, Butov LV, Novoselov KS. High-temperature superfluidity with indirect excitons in van der Waals heterostructures. *Nature Communications* **5**, 4555 (2014).
22. Wu F-C, Xue F, MacDonald AH. Theory of two-dimensional spatially indirect

equilibrium exciton condensates. *Physical Review B* **92**, 165121 (2015).

23. Berman OL, Kezerashvili RY. High-temperature superfluidity of the two-component Bose gas in a transition metal dichalcogenide bilayer. *Physical Review B* **93**, 245410 (2016).
24. Debnath B, Barlas Y, Wickramaratne D, Neupane MR, Lake RK. Exciton condensate in bilayer transition metal dichalcogenides: Strong coupling regime. *Physical Review B* **96**, 174504 (2017).
25. Kennes DM*, et al.* Moiré heterostructures as a condensed-matter quantum simulator. *Nature Physics* **17**, 155-163 (2021).
26. Wu F, Lovorn T, MacDonald AH. Theory of optical absorption by interlayer excitons in transition metal dichalcogenide heterobilayers. *Physical Review B* **97**, 035306 (2018).
27. Shabani S*, et al.* Deep moiré potentials in twisted transition metal dichalcogenide bilayers. *Nature Physics*, (2021).
28. Zhang C*, et al.* Interlayer couplings, moiré patterns, and 2D electronic superlattices in $MoS_2/WSe_2$ hetero-bilayers. *Science Advances* **3**, e1601459 (2017).
29. Carr S, Fang S, Kaxiras E. Electronic-structure methods for twisted moiré layers. *Nature Reviews Materials* **5**, 748-763 (2020).
30. Chien C-C, Peotta S, Di Ventra M. Quantum transport in ultracold atoms. *Nature Physics* **11**, 998-1004 (2015).
31. Greiner M, Mandel O, Esslinger T, Hänsch TW, Bloch I. Quantum phase transition from a superfluid to a Mott insulator in a gas of ultracold atoms. *Nature* **415**, 39-44 (2002).
32. Lagoin C*, et al.* Microscopic lattice for two-dimensional dipolar excitons. *Physical Review B* **102**, 245428 (2020).
33. Lagoin C*, et al.* Quasicondensation of bilayer excitons in a periodic potential. *Physical Review Letters* **126**, 067404 (2021).
34. Combescot M, Betbeder-Matibet O, Combescot R. Bose-Einstein condensation in semiconductors: the key role of dark excitons. *Physical Review Letters* **99**, 176403 (2007).
35. Beian M*, et al.* Spectroscopic signatures for the dark Bose-Einstein condensation of spatially indirect excitons. *EPL (Europhysics Letters)* **119**, 37004 (2017).
36. Jin C*, et al.* Observation of moiré excitons in $WSe_2/WS_2$ heterostructure superlattices. *Nature* **567**, 76-80 (2019).
37. Seyler KL*, et al.* Signatures of moiré-trapped valley excitons in $MoSe_2/WSe_2$ heterobilayers. *Nature* **567**, 66-70 (2019).
38. Tran K*, et al.* Evidence for moiré excitons in van der Waals heterostructures. *Nature* **567**, 71-75 (2019).
39. Wu F, Lovorn T, MacDonald AH. Topological exciton bands in moiré

heterojunctions. *Physical Review Letters* **118**, 147401 (2017).

40. Yu H, Liu G-B, Tang J, Xu X, Yao W. Moiré excitons: From programmable quantum emitter arrays to spin-orbit–coupled artificial lattices. *Science Advances* **3**, e1701696 (2017).
41. Yu H, Wang Y, Tong Q, Xu X, Yao W. Anomalous light cones and valley optical selection rules of interlayer excitons in twisted heterobilayers. *Physical Review Letters* **115**, 187002 (2015).
42. Combescot M, Combescot R, Dubin F. Bose–Einstein condensation and indirect excitons: a review. *Reports on Progress in Physics* **80**, 066501 (2017).
43. Merkl P*, et al.* Ultrafast transition between exciton phases in van der Waals heterostructures. *Nature Materials* **18**, 691-696 (2019).
44. Liu H, Wang C, Liu D, Luo J. Neutral and defect-induced exciton annihilation in defective monolayer $WS_2$. *Nanoscale* **11**, 7913-7920 (2019).
45. Yuan L*, et al.* Twist-angle-dependent interlayer exciton diffusion in $WS_2$–$WSe_2$ heterobilayers. *Nature Materials* **19**, 617-623 (2020).
46. Liu H, Wang C, Zuo Z, Liu D, Luo J. Direct visualization of exciton transport in defective few-layer $WS_2$ by ultrafast microscopy. *Advanced Materials* **32**, 1906540 (2020).
47. Sun Z*, et al.* Excitonic transport driven by repulsive dipolar interaction in a van der Waals heterostructure. *Nature Photonics* **16**, 79-85 (2022).
48. Ivanov AL. Quantum diffusion of dipole-oriented indirect excitons in coupled quantum wells. *Europhysics Letters (EPL)* **59**, 586-591 (2002).
49. Rapaport R, Chen G, Simon S. Analysis of trapped quantum degenerate dipolar excitons. *Applied Physics Letters* **89**, 152118 (2006).
50. Krämer M, Pitaevskii L, Stringari S. Macroscopic dynamics of a trapped bose-einstein condensate in the presence of 1D and 2D optical lattices. *Physical Review Letters* **88**, 180404 (2002).
51. Shimazaki Y*, et al.* Optical signatures of periodic charge distribution in a mott-like correlated insulator state. *Physical Review X* **11**, 021027 (2021).
52. Alexeev EM*, et al.* Resonantly hybridized excitons in moiré superlattices in van der Waals heterostructures. *Nature* **567**, 81-86 (2019).

# Supplementary Files

This is a list of supplementary files associated with this preprint. Click to download.

- SupplementaryInformation.docx